Computation of trailing-edge noise at low Mach number using LES and acoustic analogy

By Meng Wang

1. Motivation and objectives

The present work is a continuation of the work described in the previous annual research briefs (Wang 1996, 1997). The objectives of the project are twofold: (1) to develop numerical prediction methods for trailing-edge noise, using a combination of large-eddy simulation (LES) and Lighthill's theory; and (2) to generate a reliable numerical database for the study of noise source mechanisms.

Trailing-edge aeroacoustics is of importance in both aeronautical and naval applications. It is, for example, related to airframe noise, rotor and propeller noise, and noise from underwater vehicles. When turbulent boundary layer eddies are convected past the trailing edge of a large (relative to acoustic wavelength) body, their aeroacoustic source characteristics are modified by the edge, and a more efficient source results (Ffowcs Williams & Hall 1970; Crighton & Leppington 1971). This scattering mechanism produces strong, broadband radiation to the far-field. If there is coherent vortex shedding, typically associated with blunt trailing edges and/or high angles of attack, tonal or narrowband noise is also present. In addition, the highly unsteady edge flow may cause low frequency vibration of an elastic strut and hence noise radiation. To determine the structural vibration modes, the space-time characteristics of surface-pressure fluctuations are frequently required as a forcing-function input.

The case under study corresponds to the experiment conducted by Blake (1975). The flow configuration is shown in Fig. 1. A flat strut with a circular leading edge and an asymmetrically beveled trailing-edge of 25 degrees is placed in a uniform stream at zero-degree angle of attack. The strut's chord is $C = 21.125h$ and span is $L = 23.5h$, where h is the thickness. The Reynolds number based on free-stream velocity U_∞ and the chord is 2.15×10^6. The free-stream Mach number $M = U_\infty/c_\infty \approx 0.088$. Statistical measurements of velocity and fluctuating surface pressure fields in the trailing-edge region are available for comparison with computational results. Acoustic measurements were not made in this experiment although they were made in a separate experiment (Blake & Gershfeld 1988) under different flow conditions, using trailing-edges similar but not identical to the one in Fig. 1.

In the next section we first summarize the LES of the near-field, which provides the acoustic source functions (the fluctuating Reynolds stress) as well as the space-time characteristics of surface pressure fluctuations. The statistics are fully converged and should supersede the preliminary results presented in Wang (1997). Next, we discuss the computation of the radiated far-field noise. The calculations are based on an integral-form solution to the Lighthill equation with a hard-wall Green's function (Ffowcs Williams & Hall 1970).

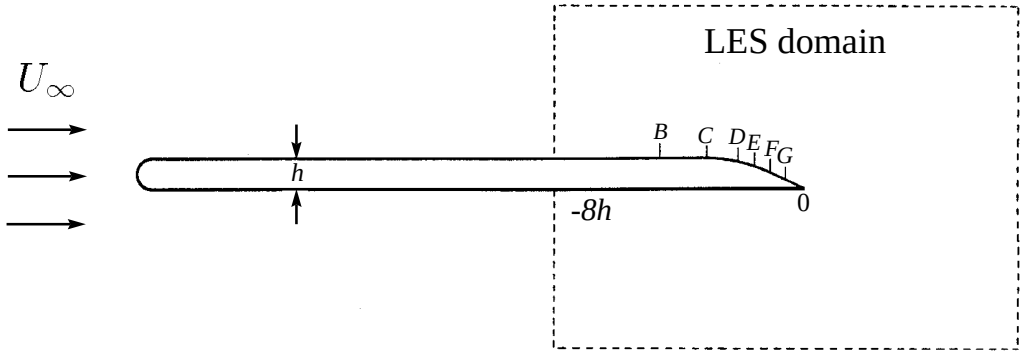

FIGURE 1. Flow configuration and computational domain. The experimental measurement stations B-G are located at $x/h = -4.625$, -3.125, -2.125, -1.625, -1.125, and -0.625, respectively.

2. Accomplishments

2.1 Update on near-field LES

2.1.1 Methodology

A detailed description of the numerical algorithm and procedure can be found in Wang (1997). The spatially filtered, unsteady, incompressible Navier-Stokes equations are solved in conjunction with the dynamic subgrid-scale model (Germano *et al.* 1991; Lilly 1992). The numerical scheme employs second-order central differences in the streamwise and wall-normal directions and Fourier collocation in the spanwise direction. A semi-implicit (Crank-Nicolson for viscous terms and third order Runge-Kutta for convective terms), fractional-step scheme is used for time advancement. The pressure Poisson equation is solved at each Runge-Kutta substep using a multi-grid iterative procedure.

Simulations are conducted in a computational domain containing the aft section of the strut and the near wake, as illustrated schematically in Fig. 1. Except for the inlet, the other three sides of the domain have been truncated for clarity. The actual domain size is approximately $16.5h$, $41h$, and $0.5h$, in the streamwise (x_1), wall normal (x_2), and spanwise (x_3) directions, respectively. The computational grid, defined in curvilinear coordinates in the x_1-x_2 plane and Cartesian coordinate in x_3, uses a total of $1536 \times 96 \times 48$ points, with appropriate clustering in the near-wall and trailing-edge regions. Of the 1536 streamwise grid points, 640 are distributed along the upper surface, 512 along the lower surface, and 2×192 along the wake line (branch cut). The maximum grid-spacing along the strut surface, measured in wall units, is $\Delta x_1^+ \approx 62$, $\Delta x_3^+ \approx 55$, and $\Delta x_2^+ \approx 2$. The simulation,

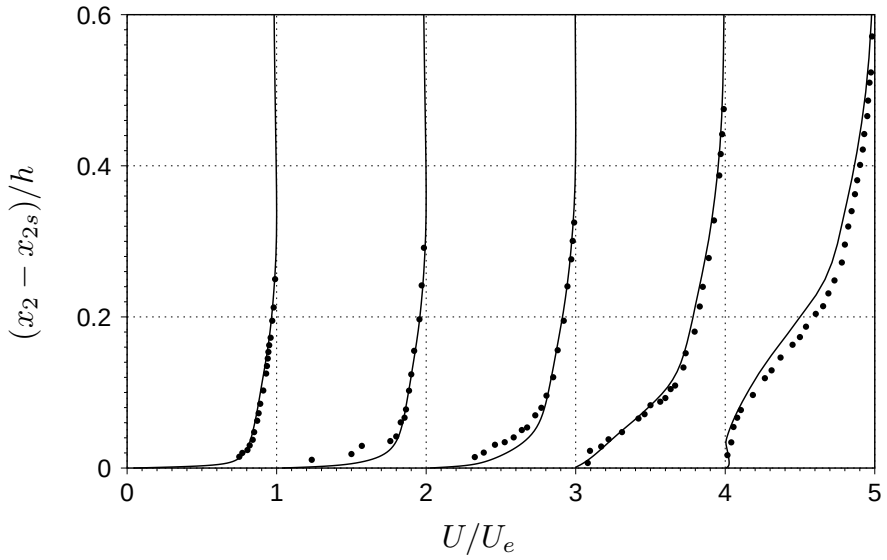

FIGURE 2. Profiles of the normalized mean velocity magnitude as a function of vertical distance from the upper surface, at stations (from left to right) C, D, E, F, and G. —— LES; • Blake's experiment. Individual profiles are separated by a horizontal offset of 1 with the corresponding zero lines located at 0, 1, ..., 4.

running at a maximum CFL number of 1.5, requires 200 single processor CPU hours on a CRAY C90 to advance one flow time across the streamwise domain length, and over 1000 CPU hours for the complete simulation. The velocity and pressure statistics presented below are collected over a period $T_s U_\infty/h \approx 60.62$, or 3.67 flow-through times based on free-stream velocity.

The inflow velocity profiles outside the boundary layers are provided by an auxiliary RANS calculation in a C-grid domain enclosing the entire strut, using Menter's (1993) SST k-ω model. Within the turbulent boundary layers, the time-dependent inflow velocities are generated from two separate LES's of flat-plate boundary layers with zero pressure gradient, using the method described by Lund, Wu & Squires (1998). The local momentum thickness and Reynolds number are matched with those from the RANS simulation. At the downstream boundary the convective outflow condition (Pauley, Moin & Reynolds 1988) is applied. The top and bottom boundaries are placed far away from the strut to minimize the impact of the imposed velocities obtained from RANS calculations. A no-slip condition is applied on the surface of the strut.

The letters B, C, D, E, F, and G in Fig. 1 indicate measurement stations in Blake's experiment. They are located at $x_1/h = -4.625$, -3.125, -2.125, -1.625, -1.125, and -0.625, respectively (the Cartesian coordinate system originates from the trailing edge). In Section 2.1.2 representative results are presented at these stations, and comparisons made with experimental values.

2.1.2 Simulation results

In Fig. 2, the magnitude of the mean velocity $U = (U_1^2 + U_2^2)^{1/2}$ normalized by its

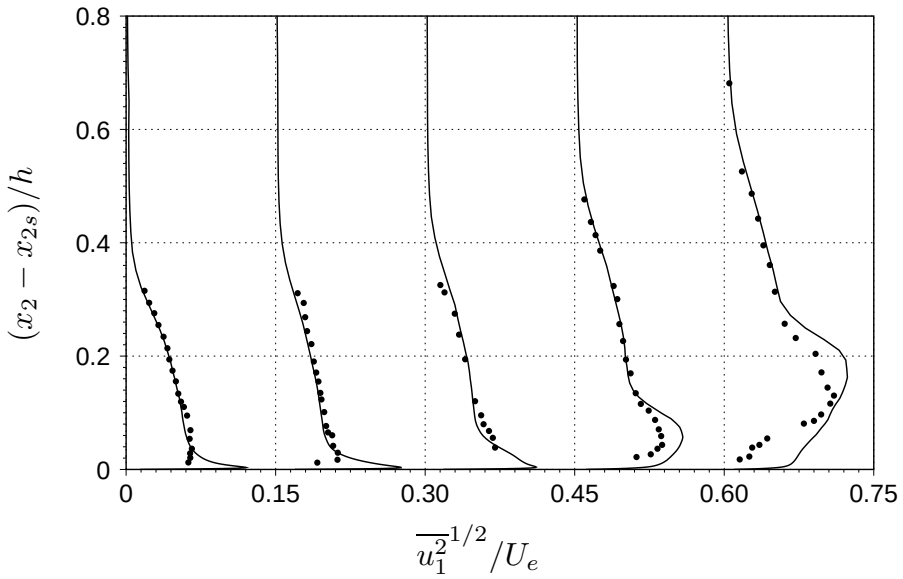

FIGURE 3. Profiles of the rms streamwise velocity fluctuations as a function of vertical distance from the upper surface, at stations (from left to right) B, D, E, F, and G. ——— LES; • Blake's experiment. Individual profiles are separated by a horizontal offset of 0.15 with the corresponding zero lines located at 0, 0.15, ..., 0.60.

value at the boundary-layer edge U_e is plotted as a function of vertical distance from the upper surface at streamwise stations (from left to right) C-G. The solid lines are from LES, and the symbols represent Blake's experimental data. Good agreement with the experimental results is obtained at station C and all the upstream locations. At stations D and E, where the boundary layer is subject to strong adverse pressure gradient (cf. Fig. 4) but remains attached to the wall, the LES profiles are more full in the near-wall region than those from the experiment. Further downstream, as an unsteady separated region develops, the discrepancy diminishes, and the computed profiles compare well again with the experimental results at stations F and G.

Figure 3 compares the computational and experimental profiles of the rms streamwise velocity fluctuations at stations (from left to right) B, D, E, F, and G. The agreement between the LES and the experimental results is quite good except in the near-wall region and at the last two stations. The experimental profiles are seen to consistently miss the near-wall peaks known to exist in turbulent boundary layers, suggesting a possible lack of spatial resolution or high-frequency response as the probe approaches the wall. The large discrepancy observed in the separated region (stations F and G) may be caused by both simulation and measurement errors. In general, hot-wire readings become increasingly difficult to interpret if the rms turbulence intensity exceeds 30% of the local mean velocity (Bradshaw 1971), which is the case in the separation bubble where the mean velocity is very small (cf. Fig. 2).

The dimensionless mean pressure ($= C_p/2$) is depicted in Fig. 4 as a function of

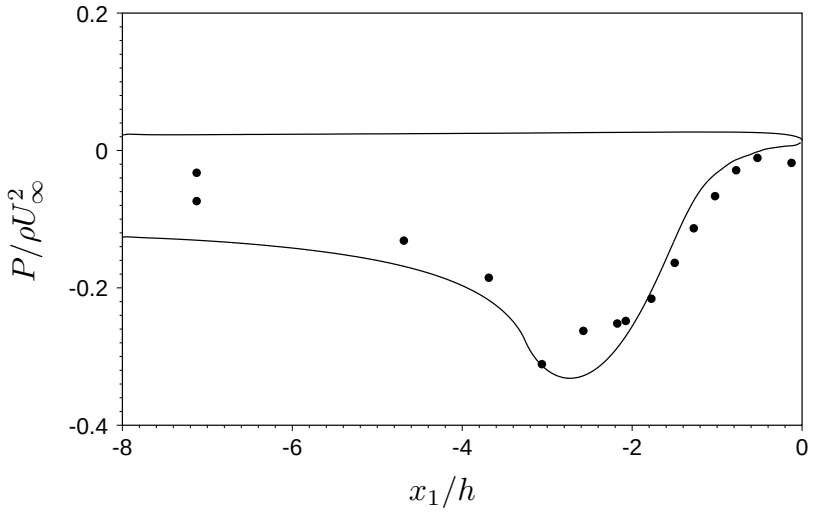

FIGURE 4. Mean surface pressure distribution near the trailing edge. —— LES; • Blake's experiment.

x_1/h. The comparison between the LES and experimental results is reasonable in the trailing-edge region but unsatisfactory upstream of it. The experimental data plotted here differ from those documented by Blake (1975) and referenced by Wang (1997) earlier. The new data set, based on the original record of his 1975 experiment, was provided by Blake (1998, private communication) after the completion of the present LES. Of particular interest is the additional data point measured on the lower surface (the upper point at $x_1/h = -7.125$ in Fig. 4), which sheds some light on the fidelity of inflow velocity conditions used in the simulation. Based on this point and assuming that the mean pressure is approximately constant on the lower surface as suggested by the LES prediction, it is evident that the lift and hence circulation in the experiment are much smaller than those in the LES. Since the circulation in the LES is imposed through the unequal mean velocity profiles on the two sides of the strut at the inlet boundary (cf. Fig. 2 in Wang 1997), one concludes that the inflow velocity difference has been exaggerated. Indeed, an estimate using C_p and the Bernoulli equation indicates that in the experiment the inflow velocities at the boundary layer edges are $U_e^{upper} \approx 1.071U_\infty$ and $U_e^{lower} \approx 1.032U_\infty$, compared with $U_e^{upper} \approx 1.093U_\infty$ and $U_e^{lower} \approx 0.979U_\infty$ used in the LES. Unfortunately, the several RANS calculations conducted earlier using different turbulence models all predict circulations much larger than the experimental value. The one chosen to provide the LES inflow profiles actually has the smallest circulation.

Figure 5 shows the space-time correlations of the upper-surface pressure fluctuations as a function of temporal and spanwise separations at stations C-G and the trailing edge (actually, one half grid spacing from the edge on the staggered mesh). The iso-correlation contours show relatively small variations of the spanwise spatial and temporal scales from stations C to E underneath the attached boundary layer with adverse pressure gradient. A dramatic increase of spatial and temporal scales occurs, however, after the turbulent boundary layer becomes separated (stations

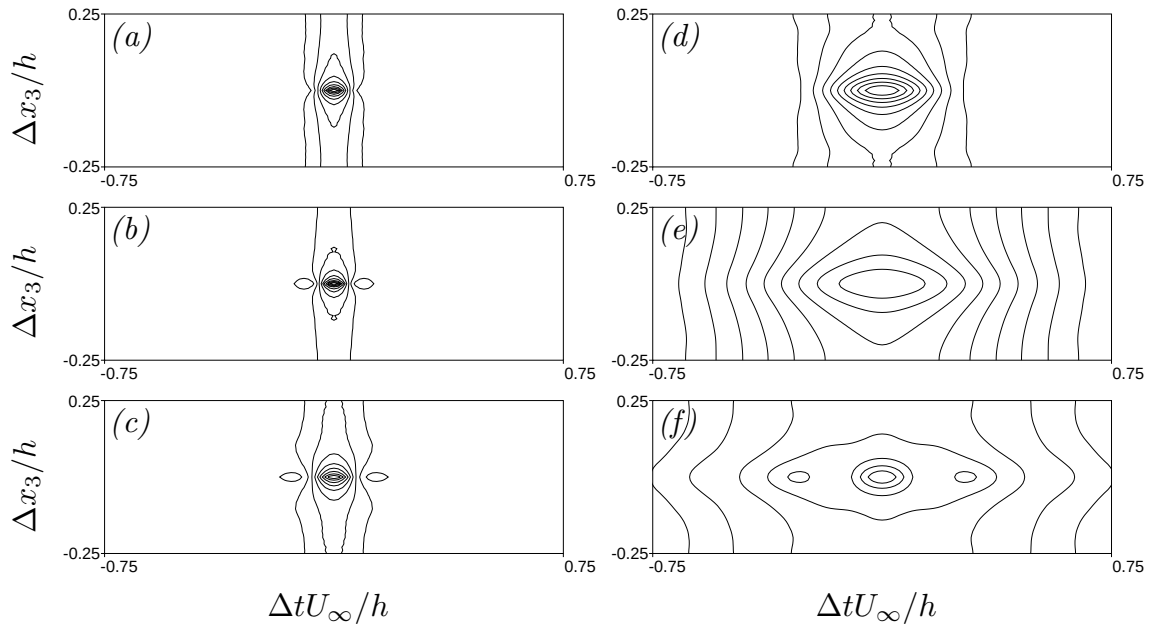

FIGURE 5. Contours of space-time correlation of the upper-surface pressure fluctuations as a function of spanwise and temporal separations, at stations (a) C; (b) D; (c) E; (d) F; (e) G; and (f) trailing-edge. Contour values are from 0.1 to 0.9, with increment 0.1.

F, G, and the trailing edge). The wall pressure fluctuations inside the separated zone are dominated by the effect of large scale fluid motion. The small scale eddies from the upstream boundary layer are lifted away from the wall and hence their contribution to the wall pressure is diminished. At the trailing edge, the correlation contours exhibit some features of small-scale correlation superimposed on the extremely large overall scales, because of the contribution from the attached boundary layer on the lower side of the edge.

It is noted that the correlation contours in Fig. 5 show insufficient drop at maximum spanwise separations inside the separated region, particularly at station G and the trailing edge. This suggests that the computational domain is too restrictive in the spanwise direction to allow the development of fully three-dimensional large-scale flow structures. The effect of the small spanwise domain size on the low-order flow statistics described above has not been investigated. In addition, it has important implications to the acoustic prediction, as will be discussed in Section 2.2.

Figure 6 depicts the frequency spectra of wall pressure fluctuations calculated from LES and compares them with those from Blake's experiment. The variables used for normalization are U_∞, h, and the dynamic pressure $q_\infty = \rho U_\infty^2/2$. The calculated spectra agree relatively well with the experimental data at most stations except station G, where the spectrum is significantly overpredicted. One notices that before the boundary layer separation (stations C-E), the LES spectra drop off more quickly than the experimental spectra at the high frequency end due to limited grid resolution and finite difference errors. The high frequency content

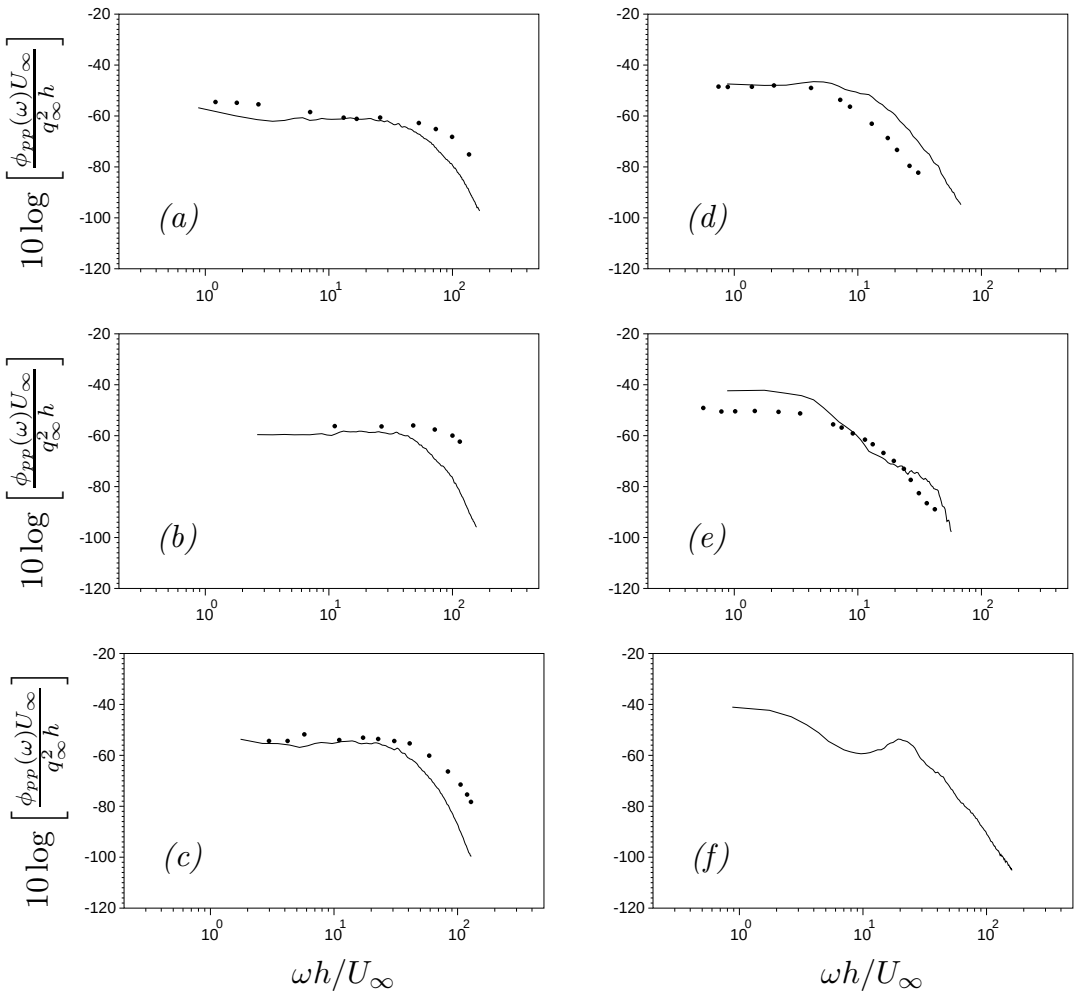

FIGURE 6. Frequency spectra of wall pressure fluctuations at stations (a) C; (b) D; (c) E; (d) F; (e) G; and (f) trailing-edge. —— LES; • experiment.

corresponds to fine spatial structures not resolved on the simulation grid. After the separation, however, the small scale effect is diminished, and the LES is capable of capturing the entire frequency range measured by the experiment. The spectrum at the trailing edge, where no experimental data are available, again consists of contributions from the upper (separated) and lower (attached) boundary layers. The latter is responsible for the high frequency peak shown in the figure.

2.2 Noise computation

2.2.1 Formulation

The noise radiation to the far-field is calculated in the framework of Lighthill's theory (Lighthill 1952). Crighton & Leppington (1971) show that the trailing-edge noise field has a non-multipole character, which is caused by the fact that the scattering surface is noncompact relative to the acoustic wavelength. To account for the surface reflection effect, a hard-wall Green's function, whose normal derivative

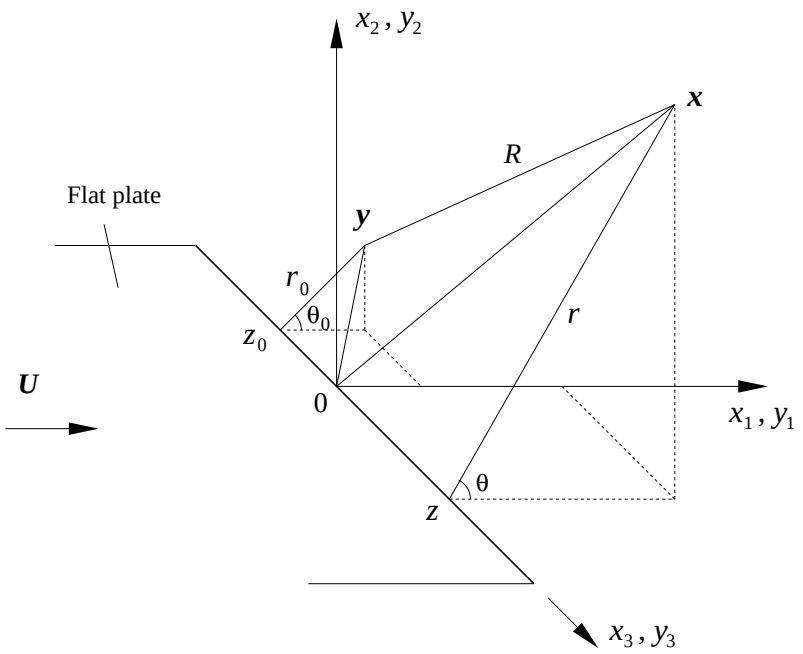

FIGURE 7. Coordinate system for calculating the radiated noise of flow past the trailing-edge of a semi-infinite flat plate.

vanishes on the surface, must be employed in an integral solution to the Lighthill equation.

When the acoustic wavelength is much longer than the thickness of the strut but much shorter than the chord ($h \ll \lambda_a \ll C$), the strut is reasonably approximated by a semi-infinite plane with zero thickness, for which the far-field Green's function is known analytically. The far-field pressure perturbation in the frequency domain can be written in the form (Ffowcs Williams & Hall 1970)

$$\widehat{p}_a(\boldsymbol{x},\omega) \approx \frac{2e^{-i\frac{\pi}{4}}}{\pi^{\frac{1}{2}}} k^2 \sin\frac{\theta}{2} \int_V \frac{e^{ikR}}{4\pi R} \frac{(\sin\phi)^{\frac{1}{2}}}{(2kr_0)^{\frac{3}{2}}} \left\{ \rho_\infty \left(\widehat{u_\theta^2 - u_r^2} \right) \sin\frac{\theta_0}{2} - 2\rho_\infty \widehat{u_r u_\theta} \cos\frac{\theta_0}{2} \right\} d^3\boldsymbol{y}. \qquad (1)$$

where the caret denotes temporal Fourier transform, ω is the circular frequency, and $k = \omega/c_\infty$ the acoustic wavenumber. The velocity components u_r and u_θ are defined in a cylindrical-polar coordinate system shown in Fig. 7. Position vectors $\boldsymbol{x}$ $(r,\ \theta,\ z)$ and $\boldsymbol{y}$ $(r_0,\ \theta_0,\ z_0)$ represent far-field and source-field points, respectively, with $R = |\boldsymbol{x} - \boldsymbol{y}|$ and $\sin\phi = r/[r^2 + (z - z_0)^2]^{\frac{1}{2}}$.

In addition to the approximate Green's function, several assumptions are implied in (1). The viscous stress is assumed unimportant as a noise source at high Reynold numbers. The convection, refraction, and scattering of acoustic waves by the turbulent flow are ignored, which is justifiable in the low Mach number limit except at very high frequencies and/or at θ values close to zero or π. Furthermore, the

integrand in (1) is derived for a source region well within one acoustic wavelength ($kr_0 \ll 1$ or $r_0 \ll \lambda_a$). Although only eddies within this distance contribute to the amplified scattering noise, from a computational point of view it may be desirable to integrate further out for better convergence (boundary-independence of the volume integral), given the $(kr_0)^{-3/2}$ decay of the Green's function factor. A more general integral expression valid for all r_0 values is given in Wang (1996). However, noise calculations using both integrals show only a small difference, and hence the simpler expression (1) will be used here.

2.2.2 Evaluation of source terms

In the context of LES, the Lighthill stress is formally expressed as $\overline{T}_{ij} = \rho\overline{u}_i\overline{u}_j + \rho\tau_{ij}$, where the overline indicates spatial filtering and the entropy and viscous terms are ignored. It consists of nonlinear interactions among resolved scales (first term) and the subgrid scale contribution to the resolved scales (second term). Piomelli, Streett, & Sarkar (1997) examined the effect of small scales on sound generation using a channel flow DNS database. In the present computation, the Lighthill stress terms are evaluated using the resolved velocity components only, assuming that the subgrid scale contribution is relatively small. It is noted that the dynamic SGS model used in the source-field simulation gives only the anisotropic part of the SGS stress tensor, $\tau_{ij} - \delta_{ij}\tau_{kk}/3$, and thus the normal stress components cannot be determined. If one desires to include $\rho\tau_{ij}$ in the noise calculation, an alternative formulation of the SGS model such as the dynamic localization model (Ghosal et al. 1995), which solves an additional equation for the subgrid-scale kinetic energy $\tau_{kk}/2$, should be used.

To compute the source terms $\widehat{u_\theta^2 - u_r^2}$ and $-2\widehat{u_r u_\theta}$ in (1), the Cartesian velocity components u_1 and u_2 on the entire computational grid are saved every 10 time steps during the source-field LES. The sampling resolution $\Delta t_s U_\infty/h \approx 0.029$. The total record of $N = 1152$ time samples, covering a period $T_s U_\infty/h \approx 33.47$, is divided into 8 segments with a 50% overlap. For each segment, which contains 256 samples, the source quantities $u_\theta^2 - u_r^2$ and $-2u_r u_\theta$ are computed. The aperiodic time series are multiplied by the Hanning window function, and discrete Fourier transforms are performed. To compensate for the energy loss due to the Hanning window tapering, the resulting Fourier coefficients are renormalized such that the power spectrum computed from them, when integrated over all positive frequencies, gives the mean-square fluctuations of the original function.

As a result of the above procedure, 8 sets of the source terms as a function of frequency ω and spatial coordinates $\boldsymbol{y}$ are available. Each set can be used in (1) to give a sample noise field. The noise power spectra are obtained as the ensemble average of the spectra from all sample fields.

Figure 8 depicts the magnitude of the Reynolds shear-stress source term (normalized), $|-2\widehat{u_r u_\theta}|/U_\infty^2$, in the trailing-edge region at 4 selected frequencies. The other source term representing the normal stress behaves in a qualitatively similar manner. The source magnitudes are averaged over the 8 samples and the spanwise direction. The contour lines show that the spatial distribution of the acoustic source varies significantly with frequency. The low frequency source, associated with the

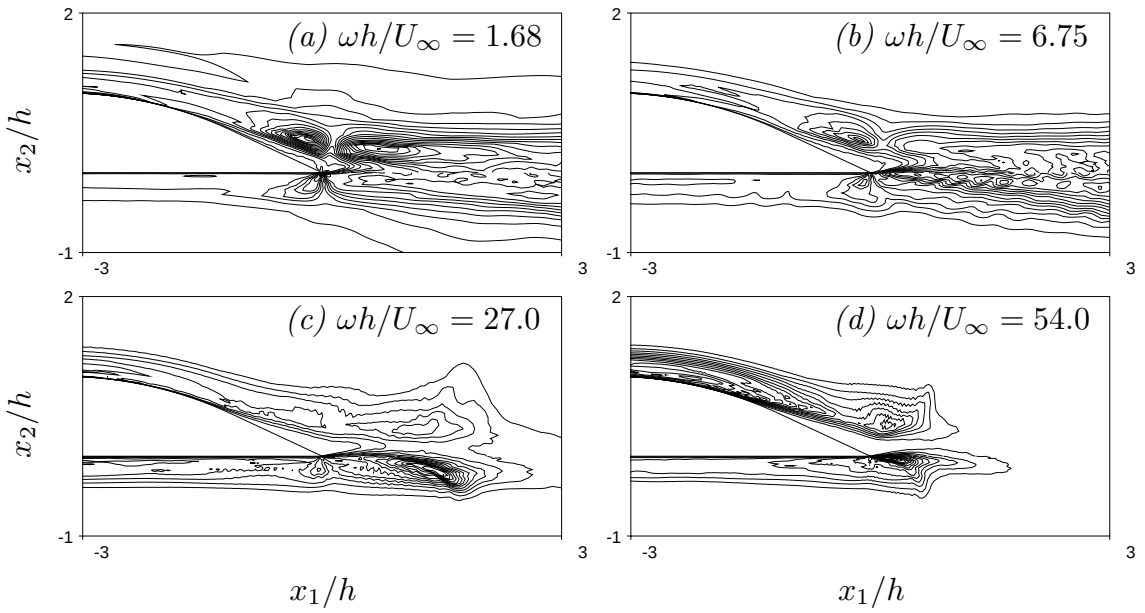

FIGURE 8. Contours of the magnitude of the acoustic source term $-2\widehat{u_r u_\theta}/U_\infty^2$ at four different frequencies. Contour levels ($\times 10^2$): (a) 0.20 to 3.40, with increment 0.20; (b) 0.20 to 3.00, with increment 0.20; (c) 0.10 to 1.40, with increment 0.10; (d) 0.03 to 0.42, with increment 0.03.

large scale unsteady flow structures, exhibits strength in a large region including the wake (cf. Figs. 8a and 8b). The largest values are found in the shear layers emanating from the upper (separated) and lower (attached) boundary layers. As the frequency increases (Figs. 8c and 8d), the source distribution becomes more concentrated, particularly in the lower shear layer close to the trailing edge. The wake region farther from the edge contributes little to the high-frequency source terms due to a lack of the corresponding small-scale flow structures. In the convolution integral (1), the source terms shown in Fig. 8 are weighted by a $(kr_0)^{-3/2}$ factor, and thus the effective noise source is much more concentrated in the trailing-eddy region.

2.2.3 Radiated field

Trailing-edge noise from a source region consisting of the computational domain can be readily obtained by evaluating the volume integral (1) numerically. As an example, Fig. 9 shows the contours of the real part of the acoustic pressure $\widehat{p}_a/P_\infty$ in the x_1-x_2 plane crossing the mid-span, for $\omega h/U_\infty = 1.68$ and 6.75. The trailing edge is located at $x_1 = x_2 = 0$, and the Mach number used in this example is $M = 0.1$. In the figure the frequency dependence of the wavelength and amplitude is evident, as is the distinct edge-noise directivity pattern dictated by the $\sin\frac{\theta}{2}$ factor in (1). The noise spectra can be obtained from the product of $\widehat{p}_a$ and its complex conjugate. It should be mentioned that Fig. 9 is based on a single sample of source functions. Statistical averaging can be done after the noise spectra from multiple source samples have been obtained.

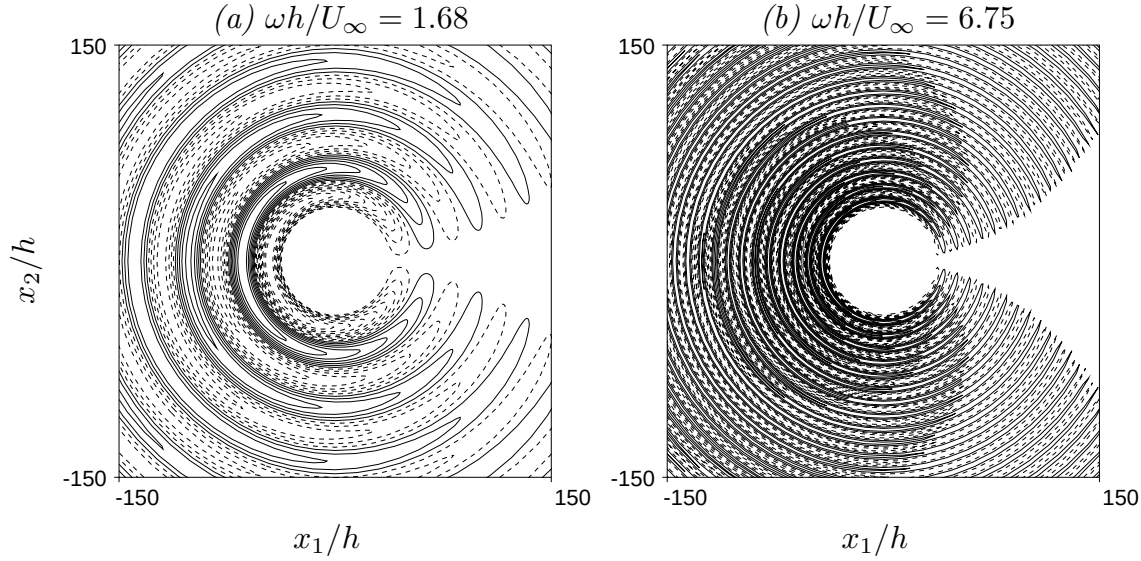

FIGURE 9. Contours of the real part of the acoustic pressure $\widehat{p}_a(\mathbf{x},\omega)/P_\infty$ from sources within the LES Domain at $M = 0.1$, at two different frequencies. Contour levels ($\times 10^6$): (a) -5.70 to 3.90, with increment 0.60; (b) -0.255 to 0.255, with increment 0.03.

In a typical LES, the spanwise width L_z of the computational domain is only a small fraction of the actual span L. For example, $L/L_z = 47$ for the present LES of Blake's experiment. To predict the frequency spectrum of the sound pressure radiated from the entire span, one requires knowledge about the spanwise coherence of the source field. Kato et al. (1993) discussed this issue in their calculation of noise from a cylinder wake. Let $\Lambda_z = \Lambda_z(\omega)$ denote the coherence length for a given frequency, two limiting cases can be found for which the total noise is well defined.

(a) If $L_z \geq \Lambda_z$, source regions separated by the computational box size radiate in a statistically independently manner. Hence, the total noise spectrum is the sum of contributions from L/L_z independent source regions along the span: $\Phi_{pa}^{total} \approx (L/L_z)\,\Phi_{pa}$.

(b) If $L \leq \Lambda_z$, the source is coherent along the entire span (2-d source). Based on (1), if the spanwise variation of the retarded time is ignored, $\widehat{p}_a^{total} \approx (L/L_z)\,\widehat{p}_a$, and hence $\Phi_{pa}^{total} \approx (L/L_z)^2\,\Phi_{pa}$.

In the intermediate regime $L_z < \Lambda_z < L$, an accurate prediction of the total sound pressure is difficult to achieve. The computational domain is too small to accommodate the spanwise flow scales, and thus the acoustic source functions are not computed reliably. The rigorous remedy is to increase the computational box size L_z so that case *a* or *b* described above applies. This is, however, often prohibitively expensive. Kato et al. (1993) resorted to an *ad hoc* approach in which Λ_z is approximated by extrapolating from the slowly-decaying coherence function, and a hybrid formula based on cases *a* and *b* is used to estimate the total noise radiation.

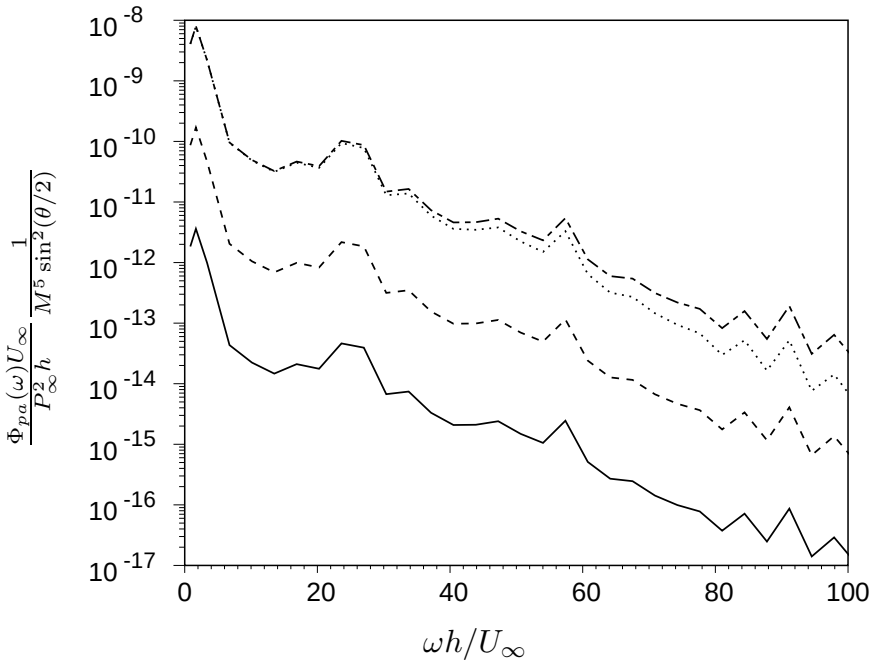

FIGURE 10. Frequency spectra of the far-field noise at $r/h = 150$ and $M = 0.088$. ——— Spectrum calculated from a partial source field (the LES domain); - - - - total spectrum assuming $L_z \geq \Lambda_z$; —·— total spectrum assuming $L \leq \Lambda_z$; ····· total spectrum using periodic source extension in span.

Another *ad hoc* approach employed by previous investigators is the periodic extension of the computed source field to the entire span. The volume integral (1) is then taken over the expanded domain. This approach is essentially equivalent to the approach used in case *b* described above except that the integration takes into account retarded-time variations along the span. Manoha, Troff & Sagaut (1998) used this method in their calculation of the noise from a blunt trailing edge of a flat plate.

In Fig. 10 several noise spectra are plotted as a function of frequency at $r/h = 150$ and $M = 0.088$. Note that the normalization factor for the spectra includes Mach number dependence and directivity. The solid line is computed from the thin slab of the source field within the LES domain. The total noise spectrum under the incoherent source assumption (case *a*) is given by the dashed line, whereas the coherence source calculation (case *b*) gives the chain-dashed line (the top curve). These two curves serve as the lower and upper bounds of the true noise spectrum. The spectrum calculated using periodic source extension in x_3, shown as the dotted curve, coincides with that from the coherence-source calculation at low frequencies but drifts to lower values at higher frequencies due to the increasing importance of retarded time variations.

The frequencies corresponding to $\lambda_a = C$ and h are given by $\omega h/U_\infty \approx 3.38$ and 71.4, respectively. They define the frequency range in which the half-plane Green's

function is approximately valid. Outside this range other appropriate Green's functions should be used. In particular, when $\lambda_a \gg C$, the strut is acoustically compact and thus the free-space Green's function is applicable. Curle's (1955) integral solution to the Lighthill equation provides a useful tool for noise computation (Wang, Lele, & Moin 1996). At high frequencies ($\lambda_a \leq h$), the Green's function must in principle be tailored to the specific trailing-edge shape. However, the potential accuracy improvement is limited, given the relatively small tip-angle of the edge and the competing high-frequency errors caused by the neglect of flow-acoustic interaction and subgrid-scale contribution to the acoustic source functions. The local spectrum peak in Fig. 10 near $\omega h/U_\infty = 23.6$ is caused by the diffraction of boundary layer eddies from the lower side.

As pointed out previously, Blake's (1975) experiment does not include acoustic measurements, and thus a direct comparison with the numerical predictions cannot be made. As a qualitative assessment, the acoustic pressure spectra from a different experiment (Blake & Gershfeld 1988) have been used to compare with the spectra shown in Fig. 10. The experimental data (not shown) are found to be concentrated at the low frequency end and lie between the coherent-source and incoherent-source predictions.

A complete determination of the far-field noise requires the spanwise coherence of the source-field to be computed. For a given field quantity q, the coherence is defined as

$$\gamma^2(\boldsymbol{x}, \boldsymbol{r}, \omega) = \frac{|\Phi_{qq}(\boldsymbol{x}, \boldsymbol{r}, \omega)|^2}{|\Phi_{qq}(\boldsymbol{x}, 0, \omega)||\Phi_{qq}(\boldsymbol{x} + \boldsymbol{r}, 0, \omega)|}, \tag{2}$$

where the cross spectrum function Φ_{qq} is the Fourier transform of the space-time cross correlation function

$$\Phi_{qq}(\boldsymbol{x}, \boldsymbol{r}, \omega) = \int_{-\infty}^{\infty} \langle q(\boldsymbol{x}, t) q(\boldsymbol{x} + \boldsymbol{r}, t + \tau) \rangle e^{-i\omega\tau} d\tau. \tag{3}$$

An estimate of γ^2 is made based on the fluctuating surface pressure ($q \equiv p$) in the vicinity of the trailing edge under the premise that it is representative of the overall coherence of the volume distribution of source terms in (1). Figure 11 shows the spanwise pressure coherence on the upper surface, one half grid spacing from the trailing edge. The left plot shows the iso-coherence contours as a function of frequency and spanwise separation. The coherence is seen to drop rapidly with spanwise separation except at the low frequency end. The coherence at selected low frequencies is depicted in the right plot as a function of spanwise separation. It is observed that for $\omega h/U_\infty \geq 5.26$, the coherence exhibits sufficient drop within the computational domain, and thus $\Phi_{pa}^{total} \approx (L/L_z)\,\Phi_{pa}$ applies. The dashed curve in Fig. 10 gives the total noise spectrum. Below this frequency, however, the coherence length is larger than the spanwise dimension of the computational box, and the total noise cannot be determined with certainty. Given the flat shape of γ^2 at large separations shown in Fig. 11 (the solid and dashed lines), it is not possible to obtain the coherence lengths by extrapolation as in the case of Kato et al. (1993).

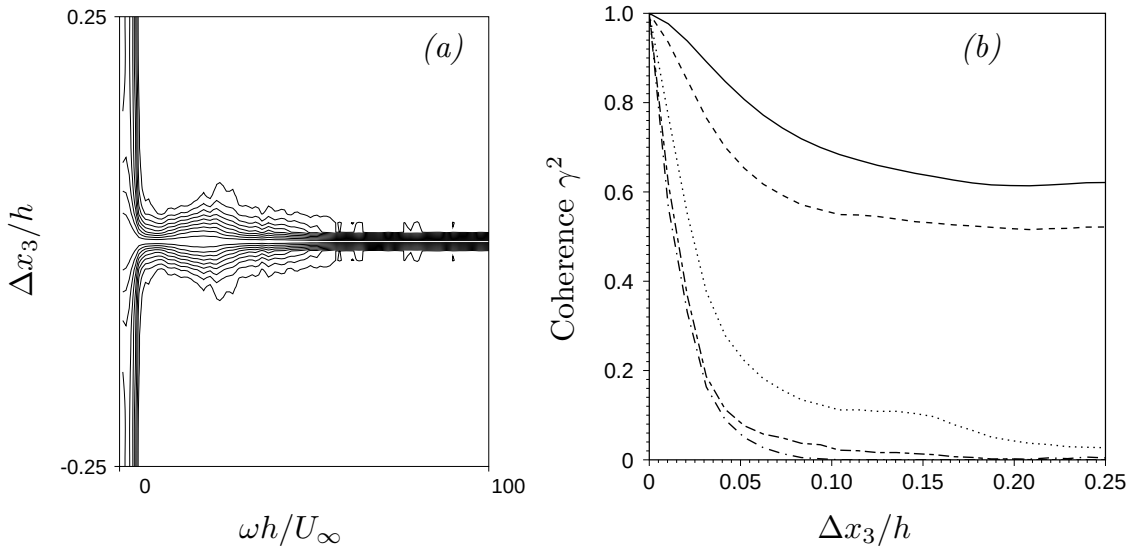

FIGURE 11. Spanwise coherence of the fluctuating surface pressure on the upper surface near the trailing edge. (a) Contour plot (contour levels from 0.1 to 0.9, with increment 0.10). (b) Coherence at frequencies $\omega h/U_\infty \approx 1.75$ (———), 3.51 (– – – –), 5.26 (·····), 7.01 (— – —), and 8.76 (— · —).

3. Summary and future work

A large-eddy simulation has been carried out for turbulent boundary layer flows past an asymmetrically beveled trailing-edge of a flat strut at a chord Reynolds number of 2.15×10^6. The asymmetric edge of 25 degree tip-angle produces a separated boundary layer on one side and an attached boundary layer on the other. The computed mean and fluctuating velocity profiles compare reasonably well with the experimental measurements of Blake (1975). The discrepancies observed at some stations (D, E for mean velocity and F, G for fluctuating velocity) may have been caused by inadequate inflow velocity conditions and small computational domain size as well as possible experimental errors near the wall and inside the separated region.

The inflow velocity profiles constitute a major uncertainty for the LES since they are not available from Blake's experiment. Based on the additional mean surface pressure data provided recently by Blake, it appears that the RANS calculations used to provide the inflow mean velocities have exaggerated the difference between velocities on the two sides of the strut, and hence the circulation. This is evidenced by the significant discrepancy between the mean surface pressure distributions from LES and the experiment.

Thus, future simulations should use more accurate inflow velocity profiles associated with a smaller circulation. The exact profiles are, however, difficult to obtain without additional experimental measurements. While it is possible to deduce from the experimental C_p data the approximate velocity magnitudes at the boundary layer edges near the inflow boundary, this approach does not give the detailed profiles extending to the outer computational boundary.

The objectives of the trailing-edge flow LES are to predict the space-time characteristics of surface pressure fluctuations and to provide the acoustic source functions for the far-field noise calculation. The frequency spectra of surface pressure fluctuations obtained from LES agree well with experimental measurements at most stations. The cause for the significant overprediction at station G needs to be further investigated. The space-time correlations of the fluctuating surface pressure demonstrate a dramatic increase in temporal and spanwise spatial scales beneath the unsteady separation region. The correlation functions near the trailing-edge show insufficient drop at maximum spanwise separations, suggesting the need for a wider computational domain.

The far-field acoustics is computed from an integral-form solution to the Lighthill equation using a hard-wall Green's function (Ffowcs Williams & Hall 1970). The Green's function is approximated by that for an infinitely thin half-plane, given the thin foil (relative to acoustic wavelength) and the small included angle of the trailing-edge. The acoustic evaluation is performed in the Fourier frequency domain and requires the storage and processing of large amount of time-dependent, three-dimensional source field data obtained from LES. Computations have been carried out to determine the source-term characteristics and the far-field noise spectra. To accurately predict the noise radiation from the entire span using a partial source field included in the LES domain, it is required that the spanwise domain size be larger than the coherence length of the source field in that direction. The present LES is found to be adequate for predicting noise radiation over a wide frequency range. At low frequencies, however, the spanwise source coherence estimated based on surface pressure fluctuations does not decay sufficiently. This issue will be addressed in future simulations using an expanded computational domain.

Acknowledgments

We gratefully acknowledge Dr. William K. Blake and Prof. Peter Bradshaw for valuable discussions during the course of this work. This work was supported by the Office of Naval Research under Grant No. N00014-95-1-0221. Computations were carried out on facilities at the DoD Major Shared Resource Center/Aeronautical Systems Center.

REFERENCES

Blake, W. K. 1975 *A Statistical Description of Pressure and Velocity Fields at the Trailing Edge of a Flat Strut*, DTNSRDC Report 4241, David Taylor Naval Ship R & D Center, Bethesda, Maryland.

Blake, W. K. & Gershfeld, J. L. 1988 The aeroacoustics of trailing edges. In *Frontiers in Experimental Fluid Mechanics,* Chapt. 10, (Gad-el-Hak, M. Eds.), Springer-Verlag.

Bradshaw, P. 1971 *An Introduction to Turbulence and Its Measurements*, Pergamon Press, Oxford.

Crighton, D. G. & Leppington, F. G. 1971 On the scattering of aerodynamic noise. *J. Fluid Mech.* **46,** 577-597.

Curle, N. 1955 The influence of solid boundaries upon aerodynamic sound. *Proc. Royal Soc. Lond.* A. **231,** 505-514.

Ffowcs Williams, J. E. & Hall, L. H. 1970 Aerodynamic sound generation by turbulent flow in the vicinity of a scattering half plane. *J. Fluid Mech.* **40,** 657-670.

Germano, M., Piomelli, U., Moin, P. & Cabot, W. H. 1991 A dynamic subgrid-scale eddy viscosity model. *Phys. Fluids A.* **3,** 1760-1765.

Ghosal, S., Lund, T. S., Moin, P., & Akselvoll, K. 1995 A dynamic localization model for large-eddy simulation of turbulent flows. *J. Fluid Mech.* **286,** 229-255.

Kato, C., Iida, A., Takano, Y., Fujita, H., & Ikegawa, M. 1993 Numerical prediction of aerodynamic noise radiated from low Mach number turbulent wake, *AIAA Paper 93-0145.*

Lighthill, M. J. 1952 On sound generated aerodynamically; I. General theory. *Proc. R. Soc. Lond.* A. **211,** 564-587.

Lilly, D. K. 1992 A proposed modification of the Germano subgrid scale closure method. *Phys. Fluids A.* **3,** 2746-2757.

Lund, T. S., Wu, X. & Squires K. D. 1998 Generation of turbulent inflow data for spatially-developing boundary layer simulations. *J. Comp. Phys.* **140,** 233-258.

Manoha, E., Troff, B., & Sagaut, P. 1998 Trailing edge noise prediction using large eddy simulation and acoustic analogy, *AIAA Paper 98-1066.*

Menter, F. R. 1993 Zonal two-equation k-ω turbulence models for aerodynamic flows, *AIAA Paper 93-2906.*

Pauley, L. L., Moin, P. & Reynolds, W. C. 1988 *Numerical Study of Unsteady Laminar Boundary Layer Separation*, Report No. TF-34, Dept. of Mech. Engr., Stanford Univ.

Piomelli, U., Streett, C. L., & Sarkar, S. 1997 On the computation of sound by large-eddy simulation. *J. Eng. Math.* **32,** 217-236.

Wang, M. 1996 Towards numerical simulations of trailing-edge aeroacoustics. *Annual Research Briefs-1996,* Center for Turbulence Research, Stanford University/NASA Ames, 133-142.

Wang, M. 1997 Progress in large-eddy simulation of trailing-edge turbulence and aeroacoustics. *Annual Research Briefs-1997,* Center for Turbulence Research, Stanford University/NASA Ames, 37-49.

Wang, M., Lele, S. K., & Moin, P 1996 Computation of quadrupole noise using acoustic analogy. *AIAA J.* **34,** 2247-2254.